2019

Exploration of High Entropy Ceramics (HECs) with Computational Thermodynamics - A Case Study with LaMnO3±δ

Yu Zhong
Worcester Polytechnic Institute

Hooman Sabarou
Worcester Polytechnic Institute

Xiaotian yan
Worcester Polytechnic Institute

Mei Yang
Worcester Polytechnic Institute

Michael C. Gao
National Energy Technology Laboratory

See next page for additional authors

Materials and Design 182 (2019) 108060

Contents lists available at ScienceDirect

Materials and Design

journal homepage: www.elsevier.com/locate/matdes

Exploration of high entropy ceramics (HECs) with computational thermodynamics - A case study with $LaMnO_{3\pm\delta}$

Yu Zhong [a,*], Hooman Sabarou [a], Xiaotian Yan [a], Mei Yang [a], Michael C. Gao [b,c], Xingbo Liu [d], Richard D. Sisson Jr [a]

[a] Mechanical Engineering, Worcester Polytechnic Institute, Worcester 01609, USA
[b] National Energy Technology Laboratory, 1450 Queen Ave SW, Albany, OR 97321, USA
[c] Leidos Research Support Team, 626 Cochrans Mill Road, P.O. Box 10940, Pittsburgh, PA 15236, USA
[d] Mechanical & Aerospace Engineering Department, West Virginia University, Morgantown, WV 26506, USA

HIGHLIGHTS

- A new definition of HECs was proposed based on computational thermodynamics, which has fundamental differences from traditional HEAs definitions;
- The integrated defect chemistry and CALPHAD approach (CALPHADPLUS) was able to effectively investigate the mixing behavior inside HECs;
- A new methodology is developed to visualize the species mixing for potential HECs;
- Mixed ionic-electronic conductive (MIEC) can be one good application for HECs.

GRAPHICAL ABSTRACT

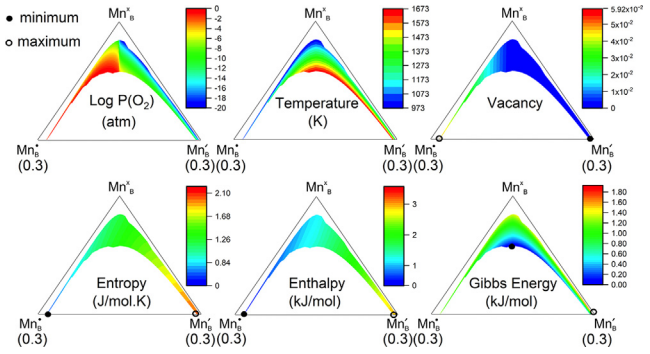

ARTICLE INFO

Article history:
Received 5 May 2019
Received in revised form 19 July 2019
Accepted 19 July 2019
Available online 19 July 2019

Keywords:
High entropy ceramics
Perovskite
Defect chemistry

ABSTRACT

The concept of the new category materials high entropy ceramics (HECs) has been proposed several years ago, which is directly borrowed from high entropy alloys (HEAs). It quickly attracts a lot of interests and displays promising properties. However, there is no clear definition of HECs differentiating it from HEAs, as it is still in its early research stage. In the current work, we are trying to use the classic perovskite $LaMnO_{3\pm\delta}$ (LMO) to demonstrate the fundamental differences between HECs and HEAs. We have adopted the integrated defect chemistry and CALPHAD approach to investigate the mixing behavior and how it is affected by the control parameters, i.e. PO_2, T, and composition. We have developed a new way to visualize the mixing behavior of the species including the cations, anions, and defects (vacancies), which linked the mixing behavior to the thermo-chemical properties including enthalpy, entropy, and Gibbs energy. It was found that entropy plays the most important role on the mixing behavior in LMO. The present work paves the way for the HECs investigation and the design of new HECs for the various applications.

1. Introduction

In conventional alloys the ductility decreases with the increase of the strength and vice versa. High entropy alloys (HEAs) are getting

* Corresponding author.
E-mail address: yzhong@wpi.edu (Y. Zhong).

https://doi.org/10.1016/j.matdes.2019.108060

significant attention due to the possibility of achieving the high ductility and high strength simultaneously [1–5]. HEAs, or multi-principal element alloys (MPEAs), complex concentrated alloys (CCA), are typically defined as alloys with 5 or more principal elements. The principal elements refer to the fraction of each component should be between 5% and 35%. In addition, "high entropy of mixing" is defined as >1.61R/mol for HEA's while "medium-entropy" is defined as 0.69R to 1.61R, though the cut-offs are sometimes used loosely. There have been a lot of investigations as shown in Fig. 1 since the concept of HEAs has been created. Various HEAs have been discovered, while some of them show promising properties. CALculation of PHAse Diagram (CALPHAD), density functional theory (DFT), and molecular dynamics (MD) are being widely used for the thermodynamic understanding of HEAs and have played critical roles on the discovery of new HEAs.

In 2012, one articles from Tsau [6] borrowed the concept of HEAs and proposed the high entropy alloy oxide, which opened the door to the investigation on the high entropy ceramics (HECs). After that, there are <70 papers published by the end of 2018. However, as Fig. 1 shows that the publications on HEAs increased significantly after the less publications in the first few years. The publications on HECs may pick up soon based on the trend in HEAs. More and more attention will be paid to the investigation of HECs. Therefore, it is important to define the HECs more clearly and find the effective ways to investigate them.

There are some interesting facts on HECs: although the first HECs article was published in 2012, its history could be tracked back to 1967. There were a couple of papers by Navrotsky and Kleppa investigating the thermodynamics including the configurational entropy, the enthalpy of formation, and cation distribution in some simple spinels [7,8]. There are also some works on oxides, carbides, nitrides, and borides with different names, i.e., entropy stabilized oxides (ESO) [9] or high entropy oxides (HEOs) [10–18] for oxides; high entropy metal diborides [19,20] for borides; high entropy carbides [21–23] for carbides; the high entropy nitrides [24–33] for nitrides. Especially, most of the investigations were based on oxides including rocksalt [9,11–13,34–38], perovskite [15,39], fluorite [15,40,41], and spinel [14]. The main research was focused on the mixing of multiple elements in HECs, i.e. mix five or more elements other than oxygen, nitrogen, carbon, or boron, sinter them, and then do XRD to verify if the single multicomponent solution phase is formed. For example, HECs based on (Mg, Ni,Co,Cu,Zn)O in rocksalt structure [9,11,34–36], $(Hf_{0.25}Zr_{0.25}Ce_{0.25}Y_{0.25})O_{2-\delta}$ in fluorite structure [15], and $Sr(Zr_{0.2}Sn_{0.2}Ti_{0.2}Hf_{0.2}Mn_{0.2})O_3$ in perovskite structure [15] were experimentally verified.

Besides the trial-and-error approach, there are a few DFT simulation papers [37,42,43] focusing on charge neutrality, electronic structure, and local atomic configurations. It is lacking on the detailed thermodynamic understanding as what has been done in HEAs. The "high entropy mixing" concept is directly borrowed from HEAs and there are no publications addressing the fundamental differences between HECs and HEAs, although it is widely aware of the existence of the multiple cations, anions, and defects besides multiple elements in ceramics. It is imperative to define HECs and understand how it is different from HEAs, especially the role of thermochemical properties including entropy, enthalpy, and Gibbs energy on HECs.

In the present paper, we use the simple $LaMnO_{3\pm\delta}$ perovskite as the case study to investigate the difference between HECs and HEAs. We develop a new methodology to visualize the species mixing and its correlation to various thermodynamic properties and control parameters. With the efforts of the present work, we attempt to establish an effective way to investigate the thermodynamics of HECs and propose a specific definition for HECs. It may pave the way to design new HECs with desired properties.

2. Thermodynamic investigation of HECs

2.1. Crystal structure and defect reactions

Similar to alloys, the crystal structure is one critical criterion to choose the thermodynamic model for ceramics. Different from the metal alloys, the other critical criterion for ceramics is the role of defect chemistry, which is closely related to the crystal structure and to be explained below by using perovskite oxide $LaMnO_{3\pm\delta}$ (LMO) as an example.

The typical perovskite oxides can be presented as ABO_3 as shown in Fig. 2. It can be seen that perovskites have three different sites, i.e. A site, which is the body center of this cubic unit cell; B site, which locates at the corner of the unit cell; and O site, which sits at the middle of two B site locations. The typical A site elements include La, Sr, Ca. The typical B site elements include Mn, Co, Cr, Fe. Using $LaMnO_{3\pm\delta}$ (LMO) as an example, it is believed that lanthanum cation La^{3+} (denoted as $La_A^{\times}$) and A

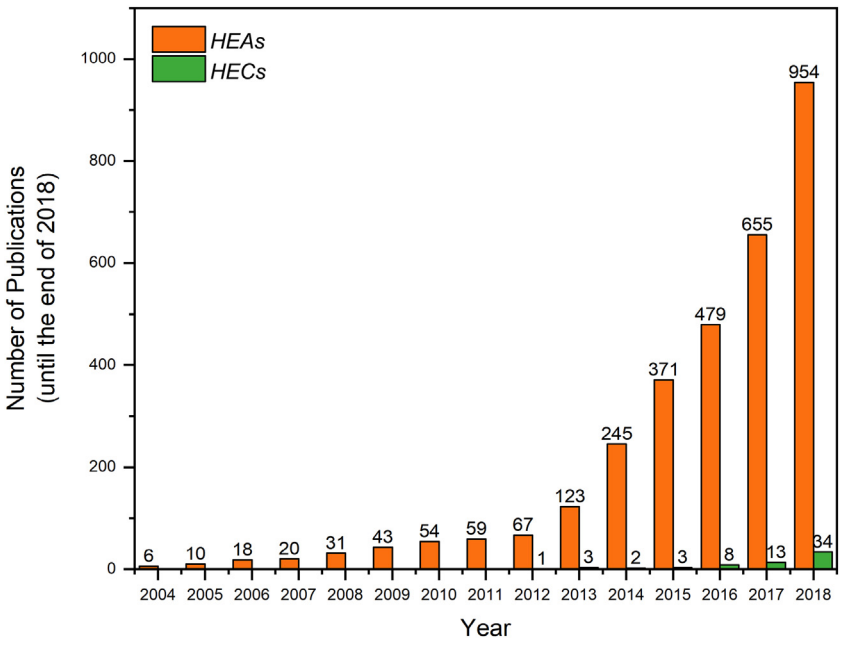

Fig. 1. Comparison of Journal Publications of HEAs and HECs till the end of 2018.

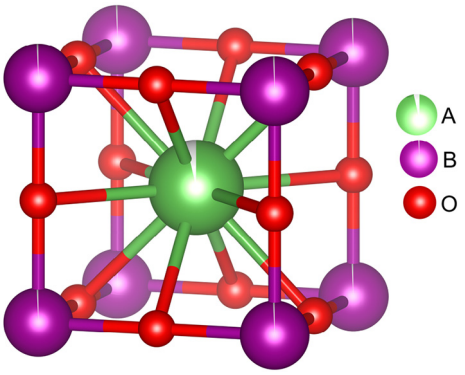

Fig. 2. The crystal structure of ABO_3 perovskite.

site vacancy (denoted as V_A'') will mainly occupy A site, meanwhile, it is suspected that very little amount of manganese cation Mn^{3+} (denoted as $Mn_A^{\times}$) exists in A site. Manganese cations Mn^{2+} (denoted as Mn_B'), Mn^{3+} (denoted as $Mn_B^{\times}$), Mn^{4+} (denoted as $Mn_B^{\bullet}$), and B site vacancy (denoted as V_B'') occupy the B site. $Mn_A^{\times}$ is called antisite defect, because Mn is traditionally treated as a B site element. The O site can be occupied by oxygen anion O^{2-} (denoted as $O_O^{\times}$) and O site vacancy (denoted as $V_O^{\bullet\bullet}$). The notation in brackets follows the Kröger-Vink notation in defect chemistry. The subscript specifies the site where the ions are located, the superscript specify the charge compared with the nominal charge of that site without the consideration of defects. $\times$ is neutral, $'$ is -1, and $\bullet$ is $+1$.

Therefore, different from the mixing of multiple elements in HEAs, the "high entropy mixing" behavior in HECs could be described as the mixing of multiple species, which include cations, anions, and defects.

There are various defect reactions within perovskites. In LMO, there are three dominant defect reactions, i.e. the reduction reaction as shown in Eq. (1) provides extra Mn_B' and $V_O^{\bullet\bullet}$; the oxidation reaction as shown in Eq. (2) provides extra $Mn_B^{\bullet}$, V_A'', V_B'', and $O_O^{\times}$; and the charge disproportionation, which provides a pair of Mn_B' and $Mn_B^{\bullet}$ ions with two $Mn_B^{\times}$ ions.

$$\frac{1}{2}O_O^{\times} + Mn_B^{\times} = \frac{1}{2}V_O^{\bullet\bullet} + Mn_B' + \frac{1}{4}O_2(gas)\ (\text{Reduction Reaction}) \quad (1)$$

$$2Mn_B^{\times} + \frac{1}{2}O_2(gas) = 2Mn_B^{\bullet} + \frac{1}{3}V_A''' + \frac{1}{3}V_B''' + O_O^{\times}(\text{Oxidation Reaction}) \quad (2)$$

$$2Mn_B^{\times} = Mn_{Mn}^{\bullet} + Mn_B'\ (\text{Charge Disproportionation}) \quad (3)$$

In the following content, we use the classic LMO perovskite as a case study to show the thermodynamic modeling effort and the critical role of the defect chemistry on the "high entropy mixing" effect of HECs.

2.2. Integrated defect chemistry analysis and CALPHAD approach

The classic CALPHAD approach pioneered by Kaufman [44] models complex phase equilibria in multicomponent alloys through computer coupling of phase diagrams and thermochemistry [44,45]. Its theoretical basis is the thermodynamic description of individual phases, including the stoichiometric compounds and solution phases. Especially, the CALPHAD approach used the following universal formula to describe the Gibbs energy of multicomponent solution phases.

$$G_m = {}^{o}G_m + \Delta^{ideal}G_m + \Delta^{xs}G_m \quad (4)$$

where is the Gibbs energy of a mechanical mixture of pure components, $\Delta^{ideal}G_m$ denotes the contribution from configurational entropy of mixing, and is the excess Gibbs energy due to interactions between the components, which is used to describe the mixing behavior other than the ideal mixing. This formula can be used to describe the gas phase, liquid phase, and also the solid solution phases. In general, for the solid solution phases, their thermodynamic model is determined by the crystal structure. The Gibbs energy can be determined by fitting the phase stability data, including liquidus, solidus, and the thermochemical data, including enthalpy, entropy, heat capacity.

It has been repeatedly proved that only the model which represents the defect chemistry of oxide solution phases can match the experimental data. LMO was modeled using the compound-energy formalism [46] to describe the mixing of ions and vacancies on three lattice sites (sublattices), $(La^{3+},Mn^{3+},Va)_1(Mn^{2+},Mn^{3+},Mn^{4+},Va)_1(O^{2-},Va)_3$, where Va stands for vacancy and subscripts 1, 1, and 3 denote the number of site for each sublattice, respectively. The current model for LMO is actually the result of extensive comparisons of various different models. As an example, the first try of LMO modeling was to decide whether random solution model or associate model should be used. The associate model was used to simulate the existence of the possible clusters that many people suspected previously in this system [47,48]. By using the integrated defect chemistry analysis and CALPHAD approach, it was found that there is no existence of clusters and only random mixing exists in LMO [48]. The second try was to determine the species in the random solution model. There were four different models considered including the consideration of Mn_B' and the addition of antisite defects, in which three different scenarios had been discussed, i.e. no antisite defects, Mn_A' as antisite defect, and $Mn_A^{\times}$ as antisite defect [49]. The integrated defect chemistry analysis and CALPHAD approach clearly ruled out the possibility of Mn_A' [49]. However, there is negligible differences with and without considering $Mn_A^{\times}$ as the antisite. The detailed comparison shows it is due to the very low concentration of $Mn_A^{\times}$ if it exists. All these detailed analyses on defect chemistry gives us the confidence of the robustness and reliability of the model determination and also the internal mixing behavior.

Using LMO as an example, there are 16 end members to model LMO without considering $Mn_A^{\times}$ as shown in Fig. 4. The three terms in Eq. (4) are written as:

$$\begin{aligned} G_m^{LaMnO_{3\pm\delta}} &= y_{La^{3+}}y_{Mn^{2+}}y_{O^{2-}}G^{LaMnO_{3\pm\delta}}_{La^{3+}:Mn^{2+}:O^{2-}} + y_{La^{3+}}y_{Mn^{3+}}y_{O^{2-}}G^{LaMnO_{3\pm\delta}}_{La^{3+}:Mn^{3+}:O^{2-}} \\ &+ y_{La^{3+}}y_{Mn^{4+}}y_{O^{2-}}G^{LaMnO_{3\pm\delta}}_{La^{3+}:Mn^{4+}:O^{2-}} + y_{La^{3+}}y_{Mn^{2+}}y_{Va}G^{LaMnO_{3\pm\delta}}_{La^{3+}:Mn^{2+}:Va} \\ &+ y_{La^{3+}}y_{Mn^{3+}}y_{Va}G^{LaMnO_{3\pm\delta}}_{La^{3+}:Mn^{3+}:Va} + y_{La^{3+}}y_{Mn^{4+}}y_{Va}G^{LaMnO_{3\pm\delta}}_{La^{3+}:Mn^{4+}:Va} + y_{La^{3+}}y_{Va}y_{O^{2-}}G^{LaMnO_{3\pm\delta}}_{La^{3+}:Va:O^{2-}} \\ &+ y_{La^{3+}}y_{Va}y_{Va}G^{LaMnO_{3\pm\delta}}_{La^{3+}:Va:Va} + y_{Va}y_{Mn^{2+}}y_{O^{2-}}G^{LaMnO_{3\pm\delta}}_{Va:Mn^{2+}:O^{2-}} + y_{Va}y_{Mn^{3+}}y_{O^{2-}}G^{LaMnO_{3\pm\delta}}_{Va:Mn^{3+}:O^{2-}} \\ &+ y_{Va}y_{Mn^{4+}}y_{O^{2-}}G^{LaMnO_{3\pm\delta}}_{Va:Mn^{4+}:O^{2-}} + y_{Va}y_{Mn^{2+}}y_{Va}G^{LaMnO_{3\pm\delta}}_{Va:Mn^{2+}:Va} + y_{Va}y_{Mn^{3+}}y_{Va}G^{LaMnO_{3\pm\delta}}_{Va:Mn^{3+}:Va} \\ &+ y_{Va}y_{Mn^{4+}}y_{Va}G^{LaMnO_{3\pm\delta}}_{Va:Mn^{4+}:Va} + y_{Va}y_{Va}y_{O^{2-}}G^{LaMnO_{3\pm\delta}}_{Va:Va:O^{2-}} + y_{Va}y_{Va}y_{Va}G^{LaMnO_{3\pm\delta}}_{Va:Va:Va} \end{aligned} \quad (5)$$

$$\begin{aligned} \Delta_{G_m^{LaMnO_{3\pm\delta}}} &= RT[(y_{La^{3+}}lny_{La^{3+}} + y_{Va}lny_{Va}) \\ &+ (y_{Mn^{3+}}lny_{Mn^{3+}} + y_{Mn^{2+}}lny_{Mn^{2+}} + y_{Mn^{4+}}lny_{Mn^{4+}} + y_{Va}lny_{Va}) \\ &+ 3(y_{O^{2-}}lny_{O^{2-}} + y_{Va}lny_{Va}) \end{aligned} \quad (6)$$

$${}^{xs}G_m = \sum_s \sum_{t\neq s} \sum_i \sum_j y_i^s y_j^t \sum_{p\neq t} \sum_m \sum_{n>m} y_m^p y_n^p \sum_{k=0}^{k} L(y_m^p - y_n^p)^k \quad (7)$$

where is the site fraction of species i in the sublattice j, is the Gibbs energy of the end member $(i)(j)(k)_3$ with the superscript $LaMnO_{3\pm\delta}$ omitted, $\Delta^{ideal}G_m$ is the ideal mixing come with the three sublattice model, is the excess Gibbs energy due to non-ideal mixing, expressed in terms of the Redlich-Kister polynomial [50], in which is the k^{th} interaction parameter between m and n in sublattice p, with i and j in sublattice s and t, respectively, and can be temperature dependent. It is worth mentioning that with considering the $Mn_A^{\times}$ antisite defects, 8 more end members need to be added.

The Gibbs energy description of each end compound in Eq. (5) is determined by the reciprocal relationships, which has been discussed

detailed in La-Mn-O system [51] and our previous publication for La-Co-O system [52]. In addition, the composition of the LMO solution phase can only move in the neutral plane as shown in Fig. 4 to keep charge neutral, which is another constraint for LMO.

The development of the perovskite thermodynamic database starts from LMO, LSM, LCO, LCF, LSF, etc. [48,49,51,53–64]. Large thermodynamic database focusing on perovskites in La-Ca-Sr-Mn-Co-Cr-Fe-O multicomponent system is available to conduct thermodynamic investigation on HECs, which contains all the efforts in the past based on integrated defect chemistry analysis and CALPHAD approach.

3. Visualization of HECs Mixing Behavior

Similar to HEAs, thermodynamics plays a critical role on HECs, which includes entropy as well as the other thermochemical properties. However, in HEAs the thermodynamic properties are related to the mixing of multiple elements while in HECs they are related to the species mixing, which includes multiple cations, anions, and defects. As shown in Fig. 5, three parameters, i.e. the oxygen partial pressure (PO_2), temperature (T), and LMO composition (i.e. A:B ratio) can change the mixing behavior in the B site of LMO through the Gibbs energy of mixing (ΔG_{mix}). In the following sections we are going to call these parameters as control parameters. ΔG_{mix} is determined by the combined effect of enthalpy of mixing (ΔH_{mix}) and entropy of mixing (ΔS_{mix}) and can be presented by the equation $\Delta G_{mix}=\Delta H_{mix}$-T$\Delta S_{mix}$.

In the present work, to show the thermodynamic properties of LMO itself, the Gibbs energies of the phases other than LMO perovskite in the La-Mn-O ternary system were not considered. The reference state was chosen as La_2O_3, MnO_2, and O_2 at each investigation temperature. The Gibbs energy of LMO is determined by the three control parameters, which is related to the B site species mixing.

We explored the impact of the control parameters within the following ranges: PO_2 from 10^{-20} to 1 atm, T from 973 K to 1673 K, and A:B ratio from 0.9 to 1.1. These parameter ranges were selected based on the interests of Solid Oxide Fuel Cell (SOFC) application. The composition of LMO with A: B = 1: 1, i.e. $La_1Mn_1O_{3\pm\delta}$, was adopted as the baseline.

In three sites of LMO, the mixing behaviors in the A site and O site are relatively simple and straightforward, because there are only 3 and 2 species in A and O sites respectively. In addition, $La_A^{\times}$ and $O_O^{\times}$ are always the dominant species in their sites. However, the mixing behavior in B site is much more complicated and of interests, which is the focus of the present work. At B site, there are four mixing species, i.e. Mn_B', $Mn_B^{\times}$, $Mn_B^{\bullet}$, and V_B''. The concentration variation of each species affects the concentrations of all the other species. Traditionally, the concentration of vacancy in each site is not clear and the contribution of vacancies on the mixing is typically neglected. Based on the thermodynamic model adopted for LMO, we can consider the contribution of vacancy in each site.

3.1. Quantitative Brouwer diagrams

It was difficult to understand the changes of the mixing in B site, especially, how the control parameters affect the mixing as well as the thermochemical properties, i.e. entropy, enthalpy, and Gibbs energy. There are various defect chemistry analysis/simulations for multicomponent oxide systems. However, it has been proven that the CALPHAD approach is the best one to tackle this problem, i.e. applying the Gibbs energy database developed by integrated defect chemistry analysis and CALPHAD (Fig. 3) to do the thermodynamic simulation. One advantage of the thermodynamic simulation by CALPHAD approach is that it can provide the quantitative Brouwer diagram [48,65], which shows the effects of control parameters on the concentration of not only the dominant species but also all the minor species.

Different from the traditional Brouwer diagram showing the concentration of species in perovskites, Fig. 6 shows the site fraction of each species quantitatively in each site of LMO with the change of PO_2 or T, which presents the species mixing behavior in specific site.

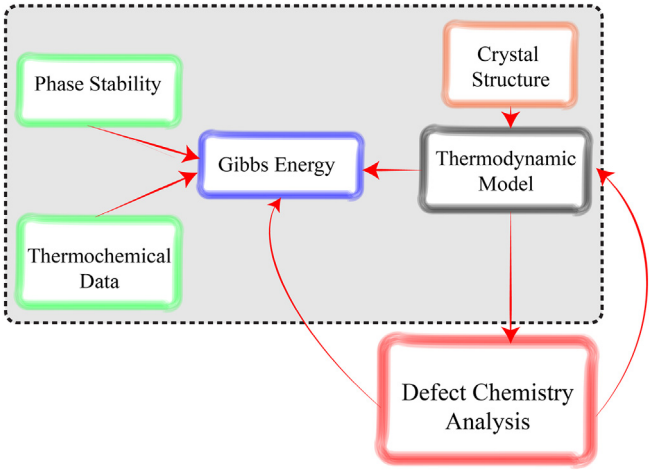

Fig. 3. The schematic of the Integrated Defect Chemistry and CALPHAD approach for HECs.

Fig. 6 (a) shows the site fraction of each species at 1173 K in A, B, and O sites as a function of PO_2, respectively. In A and O sites, $Mn_A^{\times}$ and V_A'' increase significantly, while $V_O^{\bullet\bullet}$ decreases dramatically with the increase of PO_2. Meanwhile, in B site, $Mn_B^{\times}$ is always the dominant species; while V_B'' increases, $Mn_B^{\bullet}$ increases, but Mn_B' decreases with the increase of PO_2. It can be seen that in the region that PO_2 vary from 10^{-12} to 10^{-6} atm, the concentration of $Mn_B^{\bullet}$ and Mn_B' are very close, which means the charge disproportionation dominating in this region. The oxidation reaction dominates in the region where PO_2 higher than 10^{-6} atm, while the reduction reaction dominates in the region where PO_2 lower than 10^{-12} atm.

Similarly, at $PO_2 = 0.21$ atm, in A and O sites, $Mn_A^{\times}$ does not change much, V_A'' decreases, and $V_O^{\bullet\bullet}$ increases dramatically with the increase of temperature as shown in Fig. 6 (b). Meanwhile, in B site, V_B'' decreases, $Mn_B^{\bullet}$ decreases, Mn_B' increases, and $Mn_B^{\times}$ is the dominant species and increases slightly. Overall, the control parameters, i.e. PO_2, T, and A:B ratio all affect the internal defect chemistry significantly, which changes the mixing behavior in each site and also the thermodynamic properties of LMO significantly.

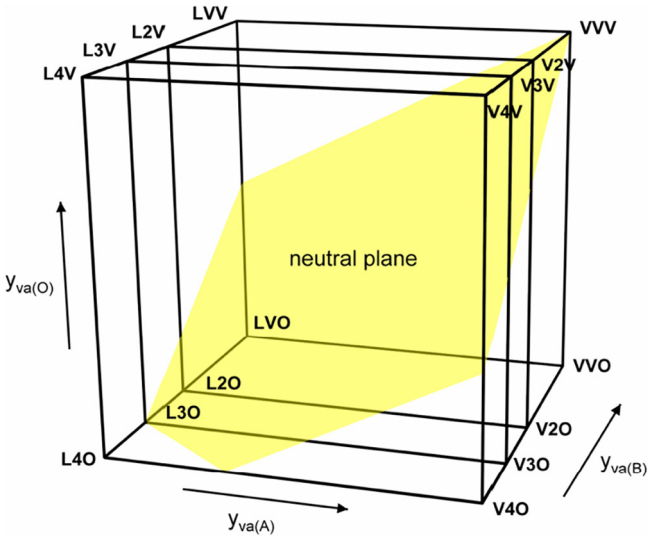

Fig. 4. Sketch for the composition space for LMO without the consideration of Mn^{3+} antisite defects $Mn_A^{\cdot}$

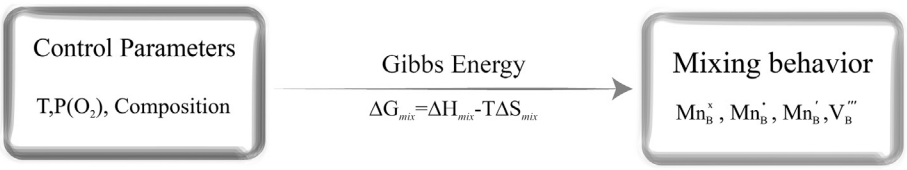

Fig. 5. Sketch of how the control parameters affecting the mixing behavior in LMO

3.2. 3-D tetrahedrons to visualize the mixing behavior in the B site

The quantitative Brouwer diagram is a powerful tool to view the concentration change of the species with the change of one specific control parameter. However, it is hard to imagine the combined role of control parameters on the mixing behavior and thermochemical properties. We created a series of 3-D tetrahedrons for the first time in the present work with the approach described in Appendix to visualize the mixing behavior of the species in B site, i.e. Mn'_B, $Mn^{\times}_B$, $Mn^{\bullet}_B$, and V''_B. Essentially, these are 3-D quantitative Brouwer diagrams for the B site species. The B site species mixing is a function of all the control parameters and the mixing space is a volume inside the tetrahedrons as shown in Fig. 7. A specific point inside the tetrahedron is corresponding to specific T, PO_2, and A:B ratio.

In the present work, we plotted the three different mixing scenarios by fixing one out of three control parameters while changing the other two to demonstrate the mixing behavior in B site. The changing ranges of control parameters are: PO_2 varies from 10^{-20} to 1 atm, T varies from 973 K to 1673 K, and A:B ratio varies from 0.9 to 1.1. By fixing one control parameter the mixing behavior is presented as a plane inside the tetrahedron. The thermochemical property, ΔS_{mix}, is selected here to show the correlation between ΔS_{mix} and the species mixing in B site, which demonstrates the "high entropy mixing" behavior of HECs.

The three mixing scenarios shown in Fig. 7 are (a) fixed A:B ratio (A:B = 1:1), (b) fixed T ($T = 1173$ K), and (c) fixed PO_2 ($PO_2 = 0.21$ atm). The bottom triangle is constructed by the ionic species, i.e. Mn'_B, $Mn^{\times}_B$, *and* $Mn^{\bullet}_B$, from which we can clearly see the mixing behavior of three different Mn ions. The lowest ΔS_{mix} is chosen as the baseline by setting it to zero, which is labeled as •, while the highest ΔS_{mix} is labeled as an open circle ◦ in each tetrahedron. In this way, we can easily see how the ΔS_{mix} change with the change of species mixing. It can be seen that the dominant species is $Mn^{\times}_B$ in most cases. The top corner of the tetrahedron is V''_B, whose contribution to the mixing behavior is hardly to be detected by traditional experimental investigations.

Fig. 7 (a) presents the mixing behavior with a fixed A:B ratio (A:B = 1:1). There are two different regions, one is the Mn'_B rich region, which is along the Mn'_B and $Mn^{\times}_B$ side. In this region, the concentration of $Mn^{\bullet}_B$ and V''_B are extremely low. The other one is the Mn'_B deficit region, in which there are very limited amount of Mn'_B. Interestingly, it can be seen that the increase of $Mn^{\bullet}_B$ brings more V''_B, which is mainly determined by Eq. (2), in which the addition of every 6 $Mn^{\bullet}_B$ ions creates 1 V''_B. Meanwhile, ΔS_{mix} increases with the increase of Mn'_B.

Fig. 7 (b) shows the mixing behavior at the fixed T, i.e. 1173 K, while the A:B ratio and PO_2 are changing. It shows the mixing plane is mainly in Mn'_B deficit region and ΔS_{mix} decrease with the increase of $Mn^{\bullet}_B$ and V''_B. Fig. 7 (c) shows the mixing behavior at the fixed PO_2, i.e. 0.21 atm. Its mixing plane is mainly in Mn'_B deficit region. Similarly, it shows ΔS_{mix} decrease with the increase of V''_B and $Mn^{\bullet}_B$.

Comparing the mixing behavior in these three different scenarios, it can be seen that the lowest ΔS_{mix} exists in the oxidation region, where there is the maximum amount of V''_B and $Mn^{\bullet}_B$. While ΔS_{mix} increases with the increase of Mn'_B and the highest ΔS_{mix} exists in the region with the maximum amount of Mn'_B. It can be concluded that ΔS_{mix} change is mainly determined by the reduction and oxidation reactions. In the oxidation region, the ΔS_{mix} increases with the decrease of V''_B, and $Mn^{\bullet}_B$, while the ΔS_{mix} increases with the increase of Mn'_B in the reduction region.

3.3. The 2-D projection of the mixing behavior in B site

The above 3-D tetrahedrons show that the thermochemical property, ΔS_{mix}, is closely related to the species mixing in B site. The control parameters i.e. PO_2, T, and A:B ratio affect the mixing behavior. However, the correlation between control parameters and mixing behavior are not shown visually in the above 3-D tetrahedrons.

To show how the control parameters impact the B site species mixing, similar 3-D tetrahedrons can be drawn. However, as the mixing is typically close to the $Mn^{\times}_B$ corner, and V''_B concentration is typically low, we can provide clearer information in 2-D projections, with the fixed A:B ratio (A:B = 1:1) to show the correlation between the B site species mixing and various factors including (a) PO_2, (b) T, (c) V''_B, (d) ΔS_{mix}, (e) ΔH_{mix}, and (f) ΔG_{mix}. In the present work, we created a series of 2-D projections (Fig. 8) to show the effects of control parameters PO_2 and T on the species mixing in B site, and the correlation between

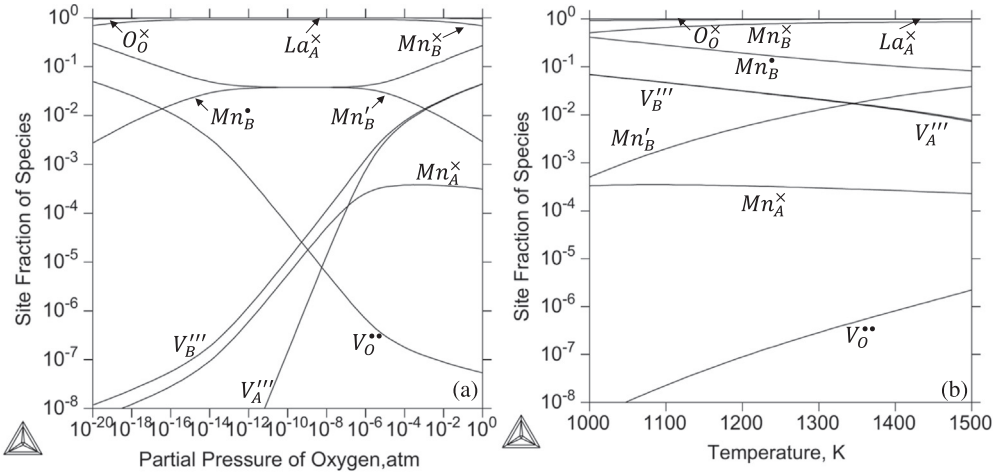

Fig. 6. the quantitative brouwer diagram of LMO (a) at 1173 K with different PO_2, (b) at $PO_2 = 0.21$ atm with different T.

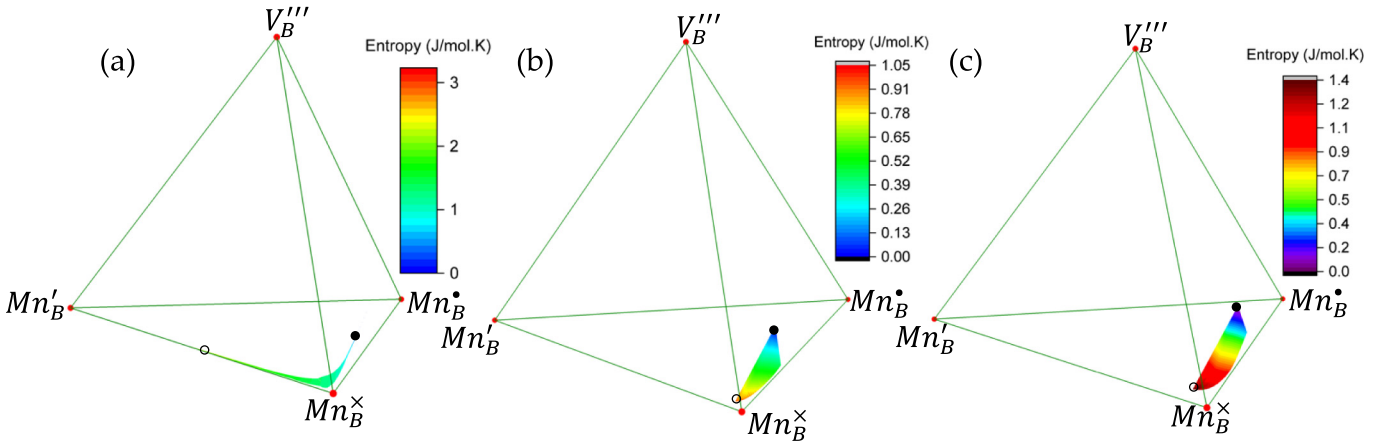

Fig. 7. The Entropy change of LMO in the 3-D space for B site mixing for LMO with different control parmaeters. The lowest ΔS_{mix} is chosen as the baseline by setting it to zero, which is labeled as •, while the highest ΔS_{mix} is labeled as an open circle ◦ in each tetrahedron: (a) The fixed A:B ratio (A:B = 1:1), (b) fixed T ($T = 1173$ K), and (c) fixed PO_2 ($PO_2 = 0.21$ atm).

the thermochemical properties and B site species mixing. For simplification, the symbols 2, 3, and 4 on the three corners represents Mn_B', $Mn_B^{\times}$, and $Mn_B^{\bullet}$. Especially, we focus on the $Mn_B^{\times}$ corner with the cutoff of 30% site fraction of $Mn_B^{\bullet}$ and Mn_B'.

Fig. 8 (a) and (b) show how PO_2 and T affect the B site mixing on the 2-D projections. It can be seen that with the increase of PO_2 the general trend is the formation of more $Mn_B^{\bullet}$. The 2-D mixing triangle can be divided into two regions, the left side with more $Mn_B^{\bullet}$ due to the dominance of oxidation reaction as shown in Eq. (2) under high PO_2 condition, while the right side is with more Mn_B' due to the dominance of reduction reaction as shown in Eq. (1) under low PO_2 condition. Meanwhile, with the increase of T the mixing moves toward the middle of the triangle, i.e. the concentration of minor species (species except $Mn_B^{\times}$) increase. Fig. 8 (c) shows the corresponding changes of the V_B'' concentration. We have labeled the lowest $V_B''$with • while the highest V_B'' with an open circle ◦. It shows the V_B'' concentration in the Mn_B' rich region is extremely low, while it greatly increases with the addition of $Mn_B^{\bullet}$. There is up to 6% V_B'' as shown in Fig. 8 (c). Overall, the formation of Mn_B' greatly reduces the formation of $Mn_B^{\bullet}$ and V_B''. In reduction condition, Mn_B' forms to keep the overall charge neutral for LMO as indicated in Eq. (1). In oxidation condition, $Mn_B^{\bullet}$ and V_B'' are formed to keep charge neutral as indicated in Eq. (2).

We can also check how the thermochemical properties including ΔS_{mix}, ΔH_{mix}, and ΔG_{mix} are affected by the change of PO_2 and T and how they are related to the species mixing of $Mn_B^{\bullet}$, $Mn_B^{\times}$, and Mn_B'. Similar to Fig. 7, the lowest entropy is chosen as the reference state, i.e. its entropy is set as zero, which is labeled with •, while the highest ΔS_{mix} is labeled with an open circle ◦ as shown in Fig. 8 (d). Same arrangement has been done for ΔH_{mix} and ΔG_{mix} as shown in Fig. 8 (e) and (f) respectively.

The correlation between ΔS_{mix} and B site mixing is shown in Fig. 8 (d). The minimum ΔS_{mix} is at the $Mn_B^{\bullet}$ rich corner while its maximum is at the Mn_B' rich corner. Fig. 8 (a) shows that the decrease of PO_2 causes the increase of Mn_B' and the decrease of $Mn_B^{\bullet}$, which leads to the decrease

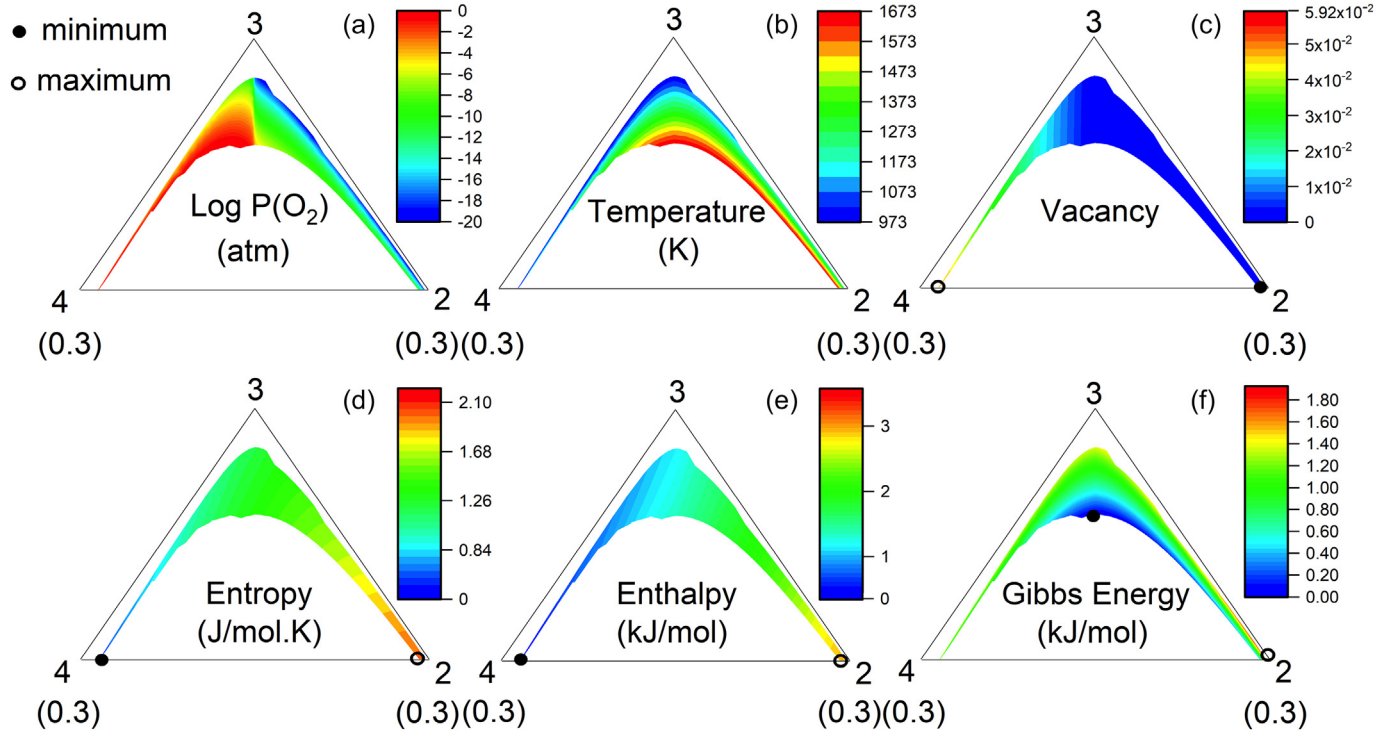

Fig. 8. 2-D mixing projections to show PO_2, T, V_B'', ΔS_{mix}, ΔH_{mix}, and ΔG_{mix} *for LMO with A:B = 1:1. the symbols 2, 3, and 4 on the three corners represents* Mn_B' $Mn_B^{\times}$, *and* $Mn_B^{\bullet}$.

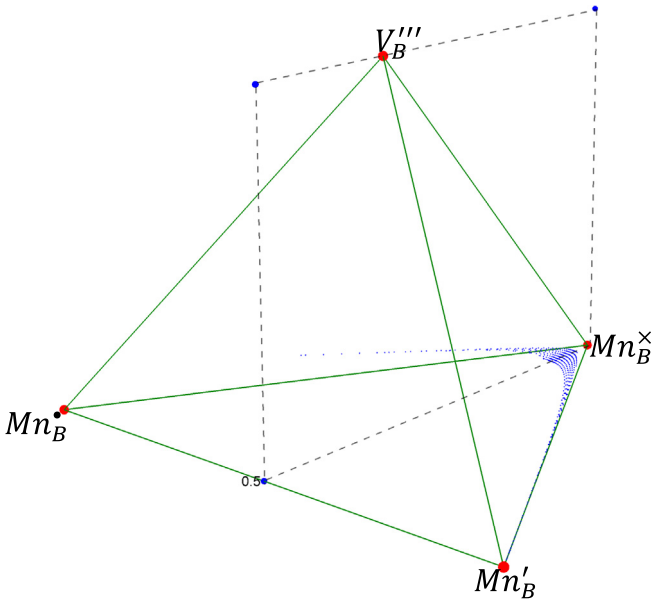

Fig. 9. "ideal" Charge disproportionation plane for LMO at different T and PO_2 inside the B site 3-D mixing tetrahedron.

of V_B'' based on Eq. (2). Therefore, the increase of ΔS_{mix} corresponds to the decrease of PO_2. Fig. 8 (e) shows ΔH_{mix} follows the similar trend. However, ΔG_{mix} decreases with the increase of T, as shown in Fig. 8 (e), which is due to the combined effect of ΔS_{mix} and ΔH_{mix}.

3.4. Charge disproportionation visualization

Charge disproportionation is widely used to understand the defect reactions in perovskites [48,52], which is imperative for the thermodynamic model determination as mentioned above. In the present work the "ideal" charge disproportionation is defined as the condition that the exact same amount of Mn_B' and $Mn_B^{\bullet}$ decomposes from $Mn_B^{\times}$ pairs. By using 3-D mixing tetrahedron the "ideal" charge disproportionation is the boundary between the reduction reaction and oxidation reaction as shown by a dash plane in Fig. 9. Based on this central plane, the side with more Mn_B' is the reduction region, while the side with more $Mn_B^{\bullet}$ is the oxidation region.

Put "ideal" charge disproportionation plane into Fig. 7 (a) the correlation between site fraction of V_B'' and site fraction of $Mn_B^{\times}$ can be plotted as shown in Fig. 10. The less site fraction of $Mn_B^{\times}$ means the more decomposition of $Mn_B^{\times}$ to Mn_B' and $Mn_B^{\bullet}$, i.e. higher charge disproportionation rate. The main y axis is the V_B'' site fraction. It can be seen that V_B'' increases with the increase of charge disproportionation rate. Meanwhile, Fig. 10 shows the variation of the other parameters including PO_2, T, ΔS_{mix}, ΔH_{mix}, and ΔG_{mix} with charge disproportionation. More importantly, $-T\Delta S_{mix}$ is appended to show the contribution of ΔS_{mix} to ΔG_{mix} of LMO. It is worth noting that the ΔS_{mix}, ΔH_{mix}, and ΔG_{mix} here are the related to the reference state selected instead of their changes in the region as used in Fig. 7 and Fig. 8. It can be seen that to reach the "ideal" charge disproportionation both PO_2 and T need to be increased. For the thermochemical data, the higher charge disproportionation rate is due to the higher ΔS_{mix} and ΔH_{mix}, which produces the lower ΔG_{mix}.

As shown in Fig. 5, $-T\Delta S_{mix}$ determines the contribution of ΔS_{mix} to ΔG_{mix}. Fig. 10 shows ΔH_{mix} is small and doesn't change much with the charge disproportionation rate, while $-T\Delta S_{mix}$ is significantly larger and is the main factor for the ΔG_{mix} changes. Essentially, this shows ΔS_{mix} plays the dominant role to greatly decrease ΔG_{mix} at higher T, which favors the further charge disproportionation.

Moreover, by using this method we can visualize and control the charge disproportionation at any specific ratio. For example, the ratios of Mn_B': $Mn_B^{\bullet}$= 1: 2 and Mn_B': $Mn_B^{\bullet}$ = 2: 1 were plotted as shown in Fig. 11 (a) and (b) to represent regions where reduction and oxidation reaction dominates respectively. In both cases, the overall trend is the same as that from the "ideal" charge disproportionation, i.e. with the increase of charge disproportionation rate more V_B'' forms, meanwhile both PO_2 and T need to be increased to satisfy the disproportionation ratios. Similarly, it shows the dramatical decrease of ΔG_{mix} with the increase of disproportionation, which is mainly due to the increase of ΔS_{mix} while ΔH_{mix} plays a much minor role.

The main differences of these two cases are: when Mn_B': $Mn_B^{\bullet}$= 1: 2, it is in the oxidation region. Its PO_2 range is higher than 10^{-8} atm and V_B'' site fraction is very high; While Mn_B': $Mn_B^{\bullet}$= 2: 1, it is in the reduction region. Its PO_2 range is lower than 10^{-7} atm and V_B'' site fraction is extremely low, which is several orders lower than that in the oxidation region.

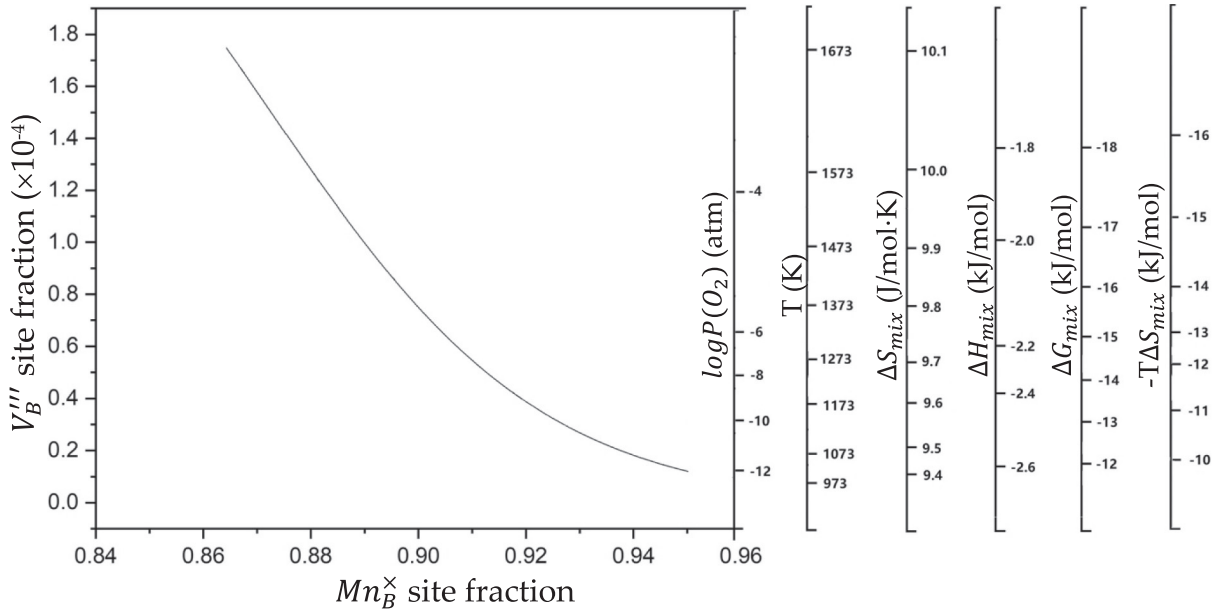

Fig. 10. "ideal" Charge disproportionation line (Mn_B': $Mn_B^{\bullet}$=1:1) for LMO at different T and PO_2, where the changes of two other control parameters $logP(O_2)$ and T, along with of ΔS_{mix}, ΔH_{mix}, ΔG_{mix}, and $-T\Delta S_{mix}$ *are attached.*

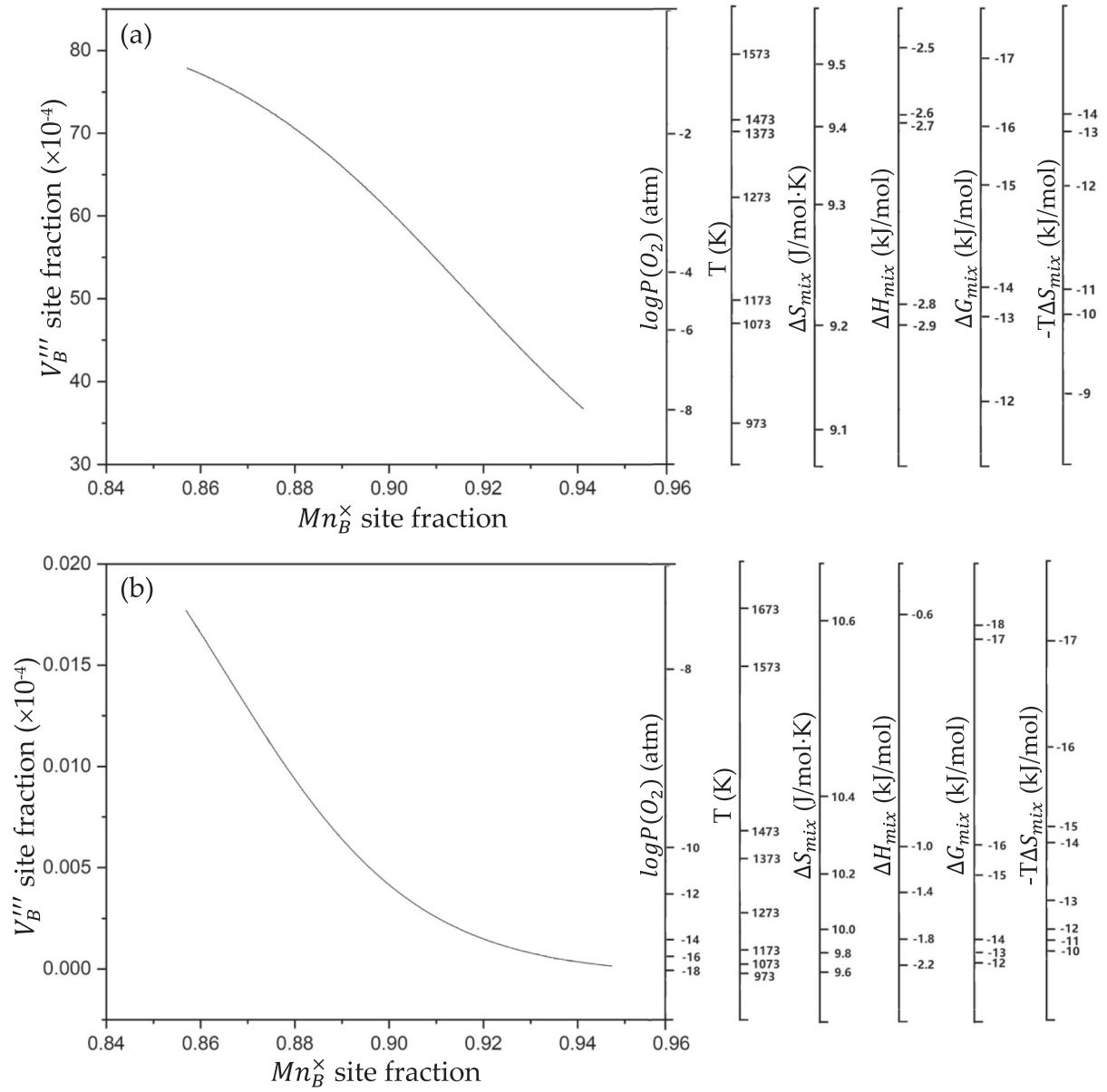

Fig. 11. Charge disproportionation lines for LMO at different T and PO_2 with (a) $Mn_B^{\prime}$: $Mn_B^{\bullet}$=1:2 and(b) 2:1, where the changes of two other control parameters log$P(O_2)$ and T, along with of ΔS_{mix}, ΔH_{mix}, ΔG_{mix}, and $-T\Delta S_{mix}$ *are attached.*

4. Discussions

4.1. Definition of HECs

Nowadays there is essentially no profound thermodynamic investigation on HECs, although HECs attract increasing interests. The "high entropy mixing" concept in previous HECs investigation was directly borrowed from HEAs. In the present work, we used LMO as a case study to understand the fundamental differences between HECs and HEAs. The following is the summary of the differences:

Firstly, the "high entropy mixing" in HEAs regards to the mixing of multiple principal elements. The principal elements are defined as the elements with concentration larger than 5 mol%. However, the "high entropy mixing" in HECs is from the mixing of multiple species including cations, anions, and defects (vacancies) in specific site. The principal species should be defined as species with concentration larger than 5% site fractions in specific site.

Secondly, it is easy to observe the mixing behavior in HEAs, as the concentration of mixing species is determined by the atomic ratios (compositions). However, in HECs, its mixing species are multiple ions and vacancies in the same lattice site with concentration determined by defect chemistry. There is no direct correlation between the concentration of mixing species and the atomic ratios (compositions).

Thirdly, the applied thermodynamic models may contain more than one sublattice in HEAs, which correspond to two or more physical sites for crystal structures such as bcc, fcc, B2, $L1_2$ etc. Typically, interaction parameters of elements in same lattice site are considered to describe the mixing behavior beyond the ideal mixing. The mixing in one site may not affect the mixing in the other site. However, the defect chemistry plays critical role in HECs. The mixing in one site of oxides surely affects the mixing in the other sites, as the oxides need to keep charge neutral. Essentially, charge neutrality provides the additional constraint on the mixing behavior in different sites.

Fourthly, the goals of "high entropy mixing" in HEAs and HECs are different. In HEAs, the focus is to increase the strength and ductility by introducing different elements and manipulating their composition, which leads to the increase of the entropy of mixing which in

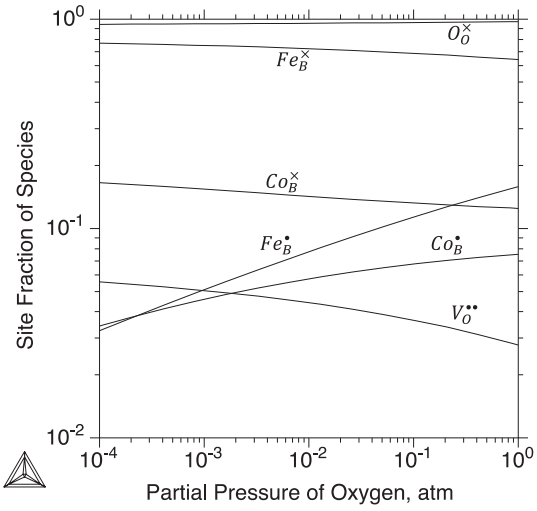

Fig. 12. The quantitative Brouwer diagram of LSCF-6428 at 1173 K with different PO_2.

turns to stabilize the multicomponent solid solution phases. While the mixing in HECs is important to various properties such as electrical, optical, and thermoelectrical properties, other than phase stabilities at different conditions. For example, LMO is a p-type semiconductor and the charge carrier for the electronic conductivity is $Mn_B^\bullet$. When the electronic mobility doesn't change much, the higher the $Mn_B^\bullet$ concentration leads to a higher the electronic conductivity [65].

Based on the comparison above, there are fundamental differences between HEAs and HECs. It is worthwhile to give a new definition of HECs, especially HEOs: the "high entropy mixing" should be among five or more dominant species including ionic species and vacancy in specific site based on the crystal structure; in which each dominant species should has >5% site fraction. It is still too early to give a criterion on entropy of mixing like what is defined in HEAs, although it does show its importance in LMO. Further investigations are needed in other perovskites and other oxides to conclude the role of entropy.

4.2. Application of the "high entropy mixing"

Based on the nature of HECs, it is not easy to get the species concentrations via the direct experimental characterizations. In the past, we are lacking the tools to investigate the mixing behavior in HECs, especially how the three control parameters (T, PO_2, and composition) affect the mixing behaviors.

With the integrated defect chemistry analysis and CALPHAD approach, and the multicomponent thermodynamic database, for the first time we have the capability to understand and control the mixing behavior in complicated multicomponent oxides, not only perovskites, but also spinel, rocksalt, fluorite. Especially, we developed the ways to visualize the species mixing in details, which specified the mixing species in HECs, the dominant role of defect chemistry, and effects of control parameters (PO_2, T, and composition) on the mixing behavior.

There are well-established theories on the relationship between defect chemistry and electronic and ionic conductivities. For example, the electronic conductivity can be expressed as:

$$\sigma_e = \sigma_n + \sigma_p = en\mu_n + ep\mu_p \tag{8}$$

where σ_n and σ_p are the electron and electron hole conductivities; n and p are the charge carrier concentrations of electrons and electron holes, respectively; and μ_n and μ_p are the charge mobilities of electrons and electron holes, respectively.

Similarly, the oxygen-ionic conductivity is related to the concentration of the carrier, i.e. oxygen vacancy ($V_O^{\bullet\bullet}$), through the following equation:

$$\sigma_O = 2e[V_O^{\bullet\bullet}]\mu_{V_O} \tag{9}$$

where *2e* is the total charge on the oxygen vacancies and μ_{V_O} is the mobility of oxygen vacancies.

In LMO, the concentration of electronic conductivity P type charge carrier, $Mn_B^\bullet$, is mainly determined by PO_2, the higher the PO_2 leads to the higher $Mn_B^\bullet$ as shown in Fig. 8. However, the behavior of the oxygen ionic conductivity charge carrier, $V_O^{\bullet\bullet}$, has the opposite trend, the higher the PO_2 leads to the lower $V_O^{\bullet\bullet}$ as shown in Fig. 6 (a). This clearly explained the intrinsic conflicts of these two conductivities. That is the reason why LMO is typically an electronic conductor, unless under extremely low PO_2 condition. However, optimizing the mixing behavior may maximize the combination of the mixed conductivity.

Based on the definition above, LMO is not HECs as it only has 4 species in B site. It was used just to demonstrate the difference between HECs and HEAs, and the approach can be applied to the investigation of HECs. However, by adding any additional B site element to LMO, there are more than four B site mixing species. If the added B site element is Co, Cr, or Fe, each one will add three ions with different valence states to create seven species mixing in B site. This meets the definition of "high entropy mixing" in HECs. Such simulations can actually be carried out on the other perovskites including the ones with more than one B site elements, such as $(La,Sr)(Co,Fe)O_{3\pm\delta}$, $(La,Sr)(Cr,Mn)O_{3\pm\delta}$, and $(La,Sr)(Cr,Fe)O_{3\pm\delta}$ with the available reliable thermodynamic database [48,49,51,53–64,66,67].

For example, With the La-Sr-Co-Fe-O thermodynamic database, the mixing behavior of $(La_{0.6}Sr_{0.4})(Co_{0.2}Fe_{0.8})O_{3\pm\delta}$ (LSCF-6428) can be predicted with the quantitative Brouwer diagram as shown in Fig. 12. It shows the mixing behavior of dominant species with site fraction larger than 1% in B site and O site at 1173 K with the change of PO_2. LSCF perovskite is modeled as $(La^{3+},Sr^{2+},Va)_1(Co^{2+},Co^{3+},Co^{4+},Fe^{2+},Fe^{3+},Fe^{4+},Va)_1(O^{2-},Va)_3$. In the B site, it has seven species and four of them have site fractions larger than 5%. Co^{4+} and Fe^{4+} are the P type charge carriers while Co^{2+} and Fe^{2+} are the n type charge carriers. It shows that the concentration of Co^{4+} and Fe^{4+} increase with PO_2, while the concentration of Co^{2+} and Fe^{2+} are too low and hence not shown in the diagram. This concludes that LSCF-6428 is a P type semiconductor. Meanwhile, its concentration of $V_O^{\bullet\bullet}$ is several orders of magnitude higher than that in LMO. This explained the reason why LSCF has much higher ionic conductivities than LMO. In addition, it shows that the concentration of $V_O^{\bullet\bullet}$ increases with the decrease of PO_2, indicating that its ionic conductivity may be much better in reducing atmosphere or in polarization condition. Of course, the mobilities (μ_n, μ_p, and μ_{V_O}) are also critical to determine the final behavior of conductivities, which probably can be calculated by DFT simulations.

5. Conclusions

Overall, we have demonstrated a new approach to investigate the "high entropy mixing" in HECs for which defect chemistry is critical. This paves the way to optimize electronic and ionic conductivities based on the concept of HECs. With this approach, we can design mixed ionic-electronic conductive (MIEC) HECs in co-doped systems. This also paves the way to design new HECs for various applications.

Meanwhile, there are several critical issues to be considered for the further investigations of HECs

1. The key of the CALPHAD approach is the Gibbs energy description of individual phases. Much more effort is needed to expand the thermodynamic database for possible HEC system;
2. Besides the MIEC properties, many other properties in ceramics are also related to the entropy of mixing. For example, improved

amorphization resistance characteristics were found in compounds that have a natural tendency to accommodate lattice disorder [68].
3. There are many properties that are related to domain formations, such as electric and magnetic susceptibilities. Besides the entropy of mixing, domain size and distributions need to be considered as well. An integrated approach with CALPHAD as demonstrated here and phase field will be more appropriated.

Credit author statement

Y.Z. Initiated the study and prepared the manuscript. H.S. and X.Y. carried out the detail simulations. M.Y., M.C.G. and X.L. organized simulation results discussion content together, and R.D.S. supervised the study. All authors participated in discussing the results and manuscript preparation.

Acknowledgement

The Author Y.Z acknowledges the financial support from the Worcester Polytechnic Institute (WPI) startup funding. The author M.C.G. acknowledges the support of the U.S. Department of Energy's Fossil Energy Cross-Cutting Technologies Program at the National Energy Technology Laboratory (NETL) under the RSS contract 89243318CFE000003.

Appendix A. Supplementary data

Supplementary data to this article can be found online at https://doi.org/10.1016/j.matdes.2019.108060.

References

[1] M.C. Gao, J.-W. Yeh, P.K. Liaw, Y. Zhang, High-Entropy Alloys, Springer, 2016.
[2] J.S. Li, W.J. Jia, J. Wang, H.C. Kou, D. Zhang, E. Beaugnon, Enhanced mechanical properties of a CoCrFeNi high entropy alloy by supercooling method, Mater Design 95 (2016) 183–187.
[3] H. Jiang, H.Z. Zhang, T.D. Huang, Y.P. Lu, T.M. Wang, T.J. Li, Microstructures and mechanical properties of Co2MoxNi2VWx eutectic high entropy alloys, Mater Design 109 (2016) 539–546.
[4] X. Xian, Z.H. Zhong, B.W. Zhang, K.J. Song, C. Chen, S. Wang, J.G. Cheng, Y.C. Wu, A high-entropy V35Ti35Fe15Cr10Zr5 alloy with excellent high-temperature strength, Mater Design 121 (2017) 229–236.
[5] W.Y. Huo, H. Zhou, F. Fang, Z.H. Xie, J.Q. Jiang, Microstructure and mechanical properties of CoCrFeNiZrx eutectic high-entropy alloys, Mater Design 134 (2017) 226–233.
[6] C.H. Tsau, Y.C. Yang, C.C. Lee, L.Y. Wu, H.J. Huang, The low electrical resistivity of the high-entropy alloy oxide thin films, Procedia Engineer 36 (2012) 246–252.
[7] A. Navrotsky, O.J. Kleppa, The thermodynamics of cation distributions in simple spinels, J. Inorg. Nucl. Chem. 29 (11) (1967) 2701–2714.
[8] A. Navrotsky, O.J. Kleppa, Thermodynamics of formation of simple spinels, J. Inorg. Nucl. Chem. 30 (2) (1968) 479–498.
[9] C.M. Rost, E. Sachet, T. Borman, A. Moballegh, E.C. Dickey, D. Hou, J.L. Jones, S. Curtarolo, J.P. Maria, Entropy-stabilized oxides, Nat. Commun. 6 (2015).
[10] D. Berardan, S. Franger, D. Dragoe, A.K. Meena, N. Dragoe, Colossal dielectric constant in high entropy oxides, Phys Status Solidi-R 10 (4) (2016) 328–333.
[11] D. Berardan, S. Franger, A.K. Meena, N. Dragoe, Room temperature lithium superionic conductivity in high entropy oxides, J. Mater. Chem. A 4 (24) (2016) 9536–9541.
[12] D. Berardan, A.K. Meena, S. Franger, C. Herrero, N. Dragoe, Controlled Jahn-Teller distortion in (MgCoNiCuZn)O-based high entropy oxides, J Alloy Compd 704 (2017) 693–700.
[13] G. Anand, A.P. Wynn, C.M. Handley, C.L. Freeman, Phase stability and distortion in high-entropy oxides, Acta Mater. 146 (2018) 119–125.
[14] J. Dabrowa, M. Stygar, A. Mikula, A. Knapik, K. Mroczka, W. Tejchman, M. Danielewski, M. Martin, Synthesis and microstructure of the (Co,Cr,Fe,Mn,Ni)(3)O-4 high entropy oxide characterized by spinel structure, Mater. Lett. 216 (2018) 32–36.
[15] S.C. Jiang, T. Hu, J. Gild, N.X. Zhou, J.Y. Nie, M.D. Qin, T. Harrington, K. Vecchio, J. Luo, A new class of high-entropy perovskite oxides, Scripta Mater 142 (2018) 116–120.
[16] A. Sarkar, L. Velasco, D. Wang, Q.S. Wang, G. Talasila, L. de Biasi, C. Kubel, T. Brezesinski, S.S. Bhattacharya, H. Hahn, B. Breitung, High entropy oxides for reversible energy storage, Nat. Commun. 9 (2018).
[17] Y. Sharma, B.L. Musico, X. Gao, C.Y. Hua, A.F. May, A. Herklotz, A. Rastogi, D. Mandrus, J.Q. Yan, H.N. Lee, M.F. Chisholm, V. Keppens, T.Z. Ward, Single-crystal high entropy perovskite oxide epitaxial films, Phys Rev Mater 2 (6) (2018).
[18] J. Gild, M. Samiee, J.L. Braun, T. Harrington, H. Vega, P.E. Hopkins, K. Vecchio, J. Luo, High-entropy fluorite oxides, J. Eur. Ceram. Soc. 38 (10) (2018) 3578–3584.
[19] J. Gild, Y. Zhang, T. Harrington, S. Jiang, T. Hu, M.C. Quinn, W.M. Mellor, N. Zhou, K. Vecchio, J. Luo, High-entropy metal diborides: a new class of high-entropy materials and a new type of ultrahigh temperature ceramics, Sci Rep-Uk 6 (2016).
[20] G. Tallarita, R. Licheri, S. Garroni, R. Orru, G. Cao, Novel processing route for the fabrication of bulk high-entropy metal diborides, Scripta Mater 158 (2019) 100–104.
[21] N.N. Guo, L. Wang, L.S. Luo, X.Z. Li, R.R. Chen, Y.Q. Su, J.J. Guo, H.Z. Fu, Microstructure and mechanical properties of in-situ MC-carbide particulates-reinforced refractory high-entropy Mo0.5NbHf0.5ZrTi matrix alloy composite, Intermetallics 69 (2016) 74–77.
[22] J. Dusza, P. Svec, V. Girman, R. Sedlak, E.G. Castle, T. Csanadi, A. Kovalcikova, M.J. Reece, Microstructure of (Hf-Ta-Zr-Nb)C high-entropy carbide at micro and nano/atomic level, J. Eur. Ceram. Soc. 38 (12) (2018) 4303–4307.
[23] E. Castle, T. Csanadi, S. Grasso, J. Dusza, M. Reece, Processing and properties of high-entropy ultra-high temperature carbides, Sci Rep-Uk 8 (2018).
[24] S.Y. Chang, Y.C. Huang, C.E. Li, H.F. Hsu, J.W. Yeh, S.J. Lin, Improved diffusion-resistant ability of multicomponent nitrides: from unitary TiN to senary high-entropy (TiTaCrZrAlRu)N, Jom-Us 65 (12) (2013) 1790–1796.
[25] M.H. Hsieh, M.H. Tsai, W.J. Shen, J.W. Yeh, Structure and properties of two Al-Cr-Nb-Si-Ti high-entropy nitride coatings, Surf Coat Tech 221 (2013) 118–123.
[26] A.D. Pogrebnjak, I.V. Yakushchenko, G. Abadias, P. Chartier, O.V. Bondar, V.M. Beresnev, Y. Takeda, O.V. Sobol, K. Oyoshi, A.A. Andreyev, B.A. Mukushev, The effect of the deposition parameters of nitrides of high-entropy alloys (TiZrHfVNb)N on their structure, composition, mechanical and tribological properties, J Superhard Mater+ 35 (6) (2013) 356–368.
[27] W.J. Shen, M.H. Tsai, K.Y. Tsai, C.C. Juan, C.W. Tsai, J.W. Yeh, Y.S. Chang, Superior oxidation resistance of (Al0.34Cr0.22Nb0.11Si0.11Ti0.22)(50)N-50 high-entropy nitride, J. Electrochem. Soc. 160 (11) (2013) C531–C535.
[28] W.J. Shen, M.H. Tsai, J.W. Yeh, Machining performance of sputter-deposited (Al0.34Cr0.22Nb0.11Si0.11Ti0.22)(50)N-50 high-entropy nitride coatings, Coatings 5 (3) (2015) 312–325.
[29] O.V. Sobol, I.V. Yakushchenko, Influence of ion implantation on the structural and stressed state and mechanical properties of nitrides of high-entropy (TiZrAlYNb)N and (TiZrHfVNbTa) N alloys, J Nano Electron Phys 7 (3) (2015).
[30] V.M. Beresnev, O.V. Sobol, S.V. Lytovchenko, U.S. Nyemchenko, V.A. Stolbovoy, D.A. Kolesnikov, A.A. Meylehov, A.A. Postelnyk, P.V. Turbin, L.V. Malikov, Effect of high-entropy components of nitride layers on nitrogen content and hardness of (TiN-Cu)/(AlNbTiMoVCr)N vacuum-arc multilayer coatings, J Nano Electron Phys 8 (2) (2016).
[31] W.L. Chen, A. Yan, X.N. Meng, D.Q. Wu, D.C. Yao, D.D. Zhang, Microstructural change and phase transformation in each individual layer of a nano-multilayered AlCrTiSiN high-entropy alloy nitride coating upon annealing, Appl. Surf. Sci. 462 (2018) 1017–1028.
[32] T.H. Hsieh, C.H. Hsu, C.Y. Wu, J.Y. Kao, C.Y. Hsu, Effects of deposition parameters on the structure and mechanical properties of high-entropy alloy nitride films, Curr. Appl. Phys. 18 (5) (2018) 512–518.
[33] T. Jin, X.H. Sang, R.R. Unocic, R.T. Kinch, X.F. Liu, J. Hu, H.L. Liu, S. Dai, Mechanochemical-assisted synthesis of high-entropy metal nitride via a soft urea strategy, Adv. Mater. 30 (23) (2018).
[34] A. Sarkar, R. Djenadic, N.J. Usharani, K.P. Sanghvi, V.S.K. Chakravadhanula, A.S. Gandhi, H. Hahn, S.S. Bhattacharya, Nanocrystalline multicomponent entropy stabilised transition metal oxides, J. Eur. Ceram. Soc. 37 (2) (2017) 747–754.
[35] C.M. Rost, Z. Rak, D.W. Brenner, J.P. Maria, Local structure of the MgxNixCoxCuxZnxO(x=0.2) entropy-stabilized oxide: an EXAFS study, J. Am. Ceram. Soc. 100 (6) (2017) 2732–2738.
[36] P.B. Meisenheimer, T.J. Kratofil, J.T. Heron, Giant enhancement of exchange coupling in entropy-stabilized oxide heterostructures, Sci Rep-Uk 7 (2017).
[37] Z. Rak, J.P. Maria, D.W. Brenner, Evidence for Jahn-Teller compression in the (Mg, Co, Ni, Cu, Zn)O entropy-stabilized oxide: a DFT study, Mater. Lett. 217 (2018) 300–303.
[38] M. Biesuz, L. Spiridigliozzi, G. Dell'Agli, M. Bortolotti, V.M. Sglavo, Synthesis and sintering of (Mg, Co, Ni, Cu, Zn)O entropy-stabilized oxides obtained by wet chemical methods, J. Mater. Sci. 53 (11) (2018) 8074–8085.
[39] A. Sarkar, R. Djenadic, D. Wang, C. Hein, R. Kautenburger, O. Clemens, H. Hahn, Rare earth and transition metal based entropy stabilised perovskite type oxides, J. Eur. Ceram. Soc. 38 (5) (2018) 2318–2327.
[40] R. Djenadic, A. Sarkar, O. Clemens, C. Loho, M. Botros, V.S.K. Chakravadhanula, C. Kubel, S.S. Bhattacharya, A.S. Gandhif, H. Hahn, Multicomponent equiatomic rare earth oxides, Mater Res Lett 5 (2) (2017) 102–109.
[41] A. Sarkar, C. Loho, L. Velasco, T. Thomas, S.S. Bhattacharya, H. Hahn, R. Djenadic, Multicomponent equiatomic rare earth oxides with a narrow band gap and associated praseodymium multivalency, Dalton T 46 (36) (2017) 12167–12176.
[42] Z. Rak, C.M. Rost, M. Lim, P. Sarker, C. Toher, S. Curtarolo, J.P. Maria, D.W. Brenner, Charge compensation and electrostatic transferability in three entropy-stabilized oxides: results from density functional theory calculations, J. Appl. Phys. 120 (9) (2016).
[43] Y.P. Wang, G.Y. Gan, W. Wang, Y. Yang, B.Y. Tang, Ab initio prediction of mechanical and electronic properties of ultrahigh temperature high-entropy ceramics (Hf0.2Zr0.2Ta0.2M0.2Ti0.2)B-2 (M=Nb, Mo, Cr), Phys Status Solidi B 255 (8) (2018).
[44] L. Kaufman, H. Bernstein, Computer Calculation of Phase Diagrams with Special Reference to Refractory Metals, Academic Press, New York, 1970.
[45] N. Saunders, A.P. Miodownik, CALPHAD (Calculation of Phase Diagrams): A Comprehensive Guide, Pergamon, Oxford ; New York, 1998.
[46] M. Hillert, B. Jansson, B. Sundman, Application of the compound-energy model to oxide systems, Z Metallkd 79 (2) (1988) 81–87.
[47] H. Yokokawa, T. Horita, N. Sakai, M. Dokiya, T. Kawada, Thermodynamic representation of nonstoichiometric lanthanum manganite, Solid State Ionics 86-8 (1996) 1161–1165.

[48] A.N. Grundy, E. Povoden, T. Ivas, L.J. Gauckler, Calculation of defect chemistry using the CALPHAD approach, Calphad 30 (1) (2006) 33–41.
[49] A.N. Grundy, B. Hallstedt, L.J. Gauckler, La1-xMn1-yO3-z perovskites modelled with and without antisite defects using the CALPHAD approach, Solid State Ionics 173 (1–4) (2004) 17–21.
[50] O. Redlich, A.T. Kister, Algebraic representations of thermodynamic properties and the classification of solutions, Ind. Eng. Chem. 40 (2) (1948) 345–348.
[51] A.N. Grundy, M. Chen, B. Hallstedt, L.J. Gauckler, Assessment of the La-Mn-O system, J Phase Equilib Diff 26 (2) (2005) 131–151.
[52] M. Yang, Y. Zhong, Z.K. Liu, Defect analysis and thermodynamic modeling of LaCoO3-delta, Solid State Ionics 178 (15–18) (2007) 1027–1032.
[53] A.N. Grundy, B. Hallstedt, L.J. Gauckler, Assessment of the La-Sr-Mn-O system, Calphad 28 (2) (2004) 191–201.
[54] M. Chen, A.N. Grundy, B. Hallstedt, L.J. Gauckler, Thermodynamic modeling of the La-Mn-Y-Zr-O system, Calphad 30 (4) (2006) 489–500.
[55] E. Povoden-Karadeniz, A.N. Grundy, M. Chen, T. Ivas, L.J. Gauckler, Thermodynamic assessment of the La-Fe-O system, J Phase Equilib Diff 30 (4) (2009) 351–366.
[56] S.H. Lee, V.R. Manga, M.F. Carolan, Z.K. Liu, Defect chemistry and phase equilibria of (La1-xCax)FeO3-delta thermodynamic modeling, J. Electrochem. Soc. 160 (10) (2013) F1103–F1108.
[57] S. Darvish, H. Sabarou, S.K. Saxena, Y. Zhong, Quantitative defect chemistry analysis and electronic conductivity prediction of La0.8Sr0.2MnO3 +/−delta perovskite, J. Electrochem. Soc. 162 (9) (2015) E134–E140.
[58] S. Darvish, S. Gopalan, Y. Zhong, Thermodynamic stability maps for the La0.6Sr0.4Co0.2Fe0.8O3 +/−delta-CO2-O-2 system for application in solid oxide fuel cells, J. Power Sources 336 (2016) 351–359.
[59] S. Darvish, Y. Zhong, S. Gopalan, Thermodynamic stability of La0.6Sr0.4Co0.2Fe0.8O3-delta in carbon dioxide impurity: a comprehensive experimental and computational assessment, in: S.C. Singhal, T. Kawada (Eds.), Solid Oxide Fuel Cells vol. 152017, pp. 1021–1025.
[60] Z.G. Lu, S. Darvish, J. Hardy, J. Templeton, J. Stevenson, Y. Zhong, SrZrO3 formation at the interlayer/electrolyte interface during (La1-xSrx)(1-delta)Co1-yFeyO3 cathode sintering, J. Electrochem. Soc. 164 (10) (2017) F3097–F3103.
[61] H. Sabarou, S. Darvish, S. Gupt, P. Singh, Y. Zhong, Thermodynamic assessment of the chemical stability of (La0.8Sr0.2)(0.98)CrxFe1 (−) (x) O-3 (+/−) (delta) under oxygen transport membrane fabrication and operation conditions, Solid State Ionics 310 (2017) 1–9.
[62] C.C. Wang, S. He, K.F. Chen, M.R. Rowles, S. Darvish, Y. Zhong, S.P. Jiang, Effect of SO2 poisoning on the electrochemical activity of La0.6Sr0.4Co0.2Fe0.8O3-delta cathodes of solid oxide fuel cells, J. Electrochem. Soc. 164 (6) (2017) F514–F524.
[63] S. Gupta, H. Sabarou, Y. Zhong, P. Singh, Phase evolution and electrochemical performance of iron doped lanthanum strontium chromite in oxidizing and reducing atmosphere, Int. J. Hydrog. Energy 42 (9) (2017) 6262–6271.
[64] S. Darvish, C.C. Wang, S.P. Jiang, Y. Zhong, Thermodynamic stability mapping and electrochemical study of La1-xSrxCo0.2Fe0.8O3 +/−delta (x=0.2-0.4) as a cathode of solid oxide fuel cells in the presence of SO2, Electrochim. Acta 287 (2018) 68–77.
[65] S. Gupta, H. Sabarou, Y. Zhong, P. Singh, Role of chromium: Iron ratio and oxygen partial pressure on the processing and chemical stability of iron doped lanthanum strontium chromite based OTM, Int. J. Hydrog. Energy 42 (40) (2017) 25351–25358.
[66] A.N. Grundy, B. Hallstedt, L.J. Gauckler, Assessment of the Sr-Mn-O system, J Phase Equilib Diff 25 (4) (2004) 311–319.
[67] S. Darvish, M. Asadikiya, B. Hu, P. Singh, Y. Zhong, Thermodynamic prediction of the effect of CO2 to the stability of (La0.8Sr0.2)(0.98)MnO3 +/−delta system, Int. J. Hydrog. Energy 41 (24) (2016) 10239–10248.
[68] K.E. Sickafus, R.W. Grimes, J.A. Valdez, A. Cleave, M. Tang, M. Ishimaru, S.M. Corish, C.R. Stanek, B.P. Uberuaga, Radiation-induced amorphization resistance and radiation tolerance in structurally related oxides, Nat. Mater. 6 (3) (2007) 217–223.